

Removal and Selection: Improving RGB-Infrared Object Detection via Coarse-to-Fine Fusion

Tianyi Zhao[†], Maoxun Yuan[†], Feng Jiang, Nan Wang, Xingxing Wei*

Abstract—Object detection in visible (RGB) and infrared (IR) images has been widely applied in recent years. Leveraging the complementary characteristics of RGB and IR images, the object detector provides reliable and robust object localization from day to night. Most existing fusion strategies directly input RGB and IR images into deep neural networks, leading to inferior detection performance. However, the RGB and IR features have modality-specific noise, these strategies will exacerbate the fused features along with the propagation. Inspired by the mechanism of the human brain processing multimodal information, in this paper, we introduce a new coarse-to-fine perspective to purify and fuse two modality features. Specifically, following this perspective, we design a Redundant Spectrum Removal module to coarsely remove interfering information within each modality and a Dynamic Feature Selection module to finely select the desired features for feature fusion. To verify the effectiveness of the coarse-to-fine fusion strategy, we construct a new object detector called the Removal and Selection Detector (RSDet). Extensive experiments on three RGB-IR object detection datasets verify the superior performance of our method. The source code and results are available at <https://github.com/Zhao-Tian-yi/RSDet.git>

Index Terms—RGB-Infrared Object Detection, Coarse-to-Fine Fusion Strategy, Multisensory Fusion, Mixture of Experts.

I. INTRODUCTION

Object detection on single modality is one of the fundamental tasks in computer vision, garnering significant attention and finding applications across diverse fields such as surveillance [1], [2], remote sensing [3]–[5], and autonomous driving [6], [7]. However, object detection methods reliant solely on one single modality have shown susceptibility to various challenges [8], like illumination, weather, adversarial attack, occlusion, etc. Therefore, the multiple sensor modalities fusion method has come into view [9]–[12]. With the development of various sensors, multimodal images are collected and applied in more and more application fields. Among them, visible (RGB) and infrared (IR) sensors are widely utilized due to their complementary imaging characteristics. Specifically, visible images can reflect rich texture and color information of

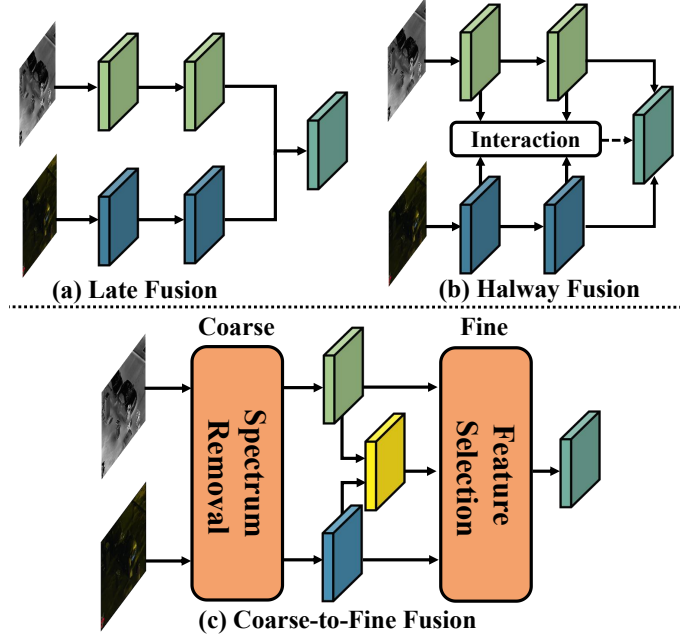


Fig. 1: Comparison between existing RGB-IR feature fusion structure and our proposed framework.

the object but are greatly affected by low-light environments. In contrast, infrared images can reflect the thermal information of the object and can clearly reflect the outline of the object under poor illumination conditions, but lack the texture details of the object. In recent years, researchers have focused on the visible and infrared feature-level fusion [13]–[17], which can help achieve better performance on downstream tasks (e.g., object detection).

In RGB-IR object detection, the effective feature fusion method of RGB and IR images is crucial. Most existing RGB-IR object detection methods extract the modality-specific features from RGB and IR images independently, and then directly perform addition or concatenation operations on these features [18]–[20], as shown in Figure 1(a). Without explicit cross-modal fusion, the “Late fusion” strategy is therefore limited in learning the complementary information, resulting in inferior performance. To further explore the optimal fusion strategies, many researchers have considered the “Halfway fusion” strategy to design an interaction module between different modality features [21]–[23], as shown in Figure 1(b). For instance, Zhou *et al.* [21] construct the DMAF module to tap the difference between RGB and IR modalities which brings more useful information at the feature level. Xie *et al.* [22] introduce a novel dynamic cross-modal module that

Corresponding author*: Xingxing Wei.

Xingxing Wei is with the Institute of Artificial Intelligence, Hangzhou Innovation Institute, Beihang University, Beijing, 100191, China (e-mail: xxwei@buaa.edu.cn).

Tianyi Zhao is with the Institute of Artificial Intelligence, Beihang University, No.37, Xueyuan Road, Haidian District, Beijing, 100191, China (e-mail: ty_zhao@buaa.edu.cn).

Maoxun Yuan is with the School of Computer Science and Engineering, Beihang University, No.37, Xueyuan Road, Haidian District, Beijing, 100191, China (e-mail: yuanmaoxun@buaa.edu.cn).

Feng Jiang and Nan Wang are with the Beijing Institute of Control and Electronic Technology, Beijing, 100038, China.

[†] represents the equal contribution to this work.

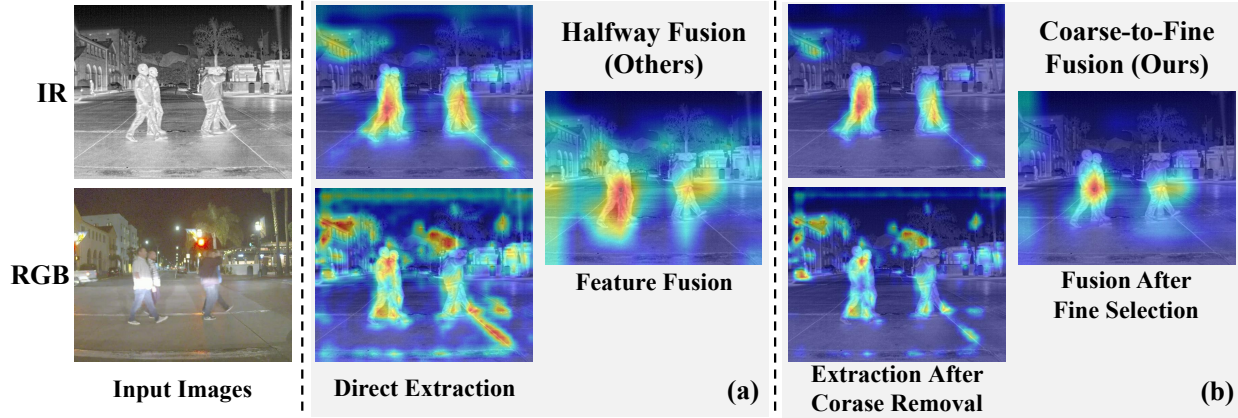


Fig. 2: Effectiveness of our Coarse-to-Fine fusion. (a) is the current Halfway Fusion method, the directly extracted features are interfered with by the background information from the RGB image and suppress the final fused features, which will result in inferior detection results. (b) Our coarse-to-fine fusion can reduce the irrelevant information and select desired features for fusion, which achieves superior performance.

aggregates local and global information from RGB and IR modalities, etc. Although these methods have achieved encouraging improvements, they ignore the negative impact of the modality-noise along with the propagation, which would fail to achieve complementary fusion.

Actually, when confronted with multi-modal information, our brains initially establish rules to filter out interfering information and then meticulously select the desired information, a process that has been modeled in cognitive theory (“Attenuation Theory” [24]). This approach can be likened to a coarse-to-fine process, inspiring us to introduce a fresh perspective for fusing RGB and IR features. As shown in Figure 1(c), we design a new fusion strategy called “Coarse-to-Fine Fusion” to achieve complementary feature fusion.

“Coarse” indicates that our method begins with the filter out the interfering information and thus can **coarsely remove** the irrelevant spectrum. To this end, since the redundant information in an image also exists in its frequency spectrum [25], we propose a Redundant Spectrum Removal (RSR) module to filter out coarsely in the frequency domain. Specifically, we convert each source image into frequency space and introduce a dynamic filter to adaptively reduce irrelevant spectrum within RGB and IR modalities. As for “Fine”, it indicates that our fusion strategy conducts **finely select** features after the coarse removal. We design a Dynamic Feature Selection (DFS) module to meticulously select the desired features between RGB and IR modalities. In this module, we weighted different scale features required for object detection by exploring a mixture of scale-aware experts. Figure 2 gives an example of our Coarse-to-Fine fusion strategy. To evaluate the effectiveness of the coarse-to-fine strategy, we build a novel framework for RGB-IR object detection called **Removal and Selection Detector (RSDet)**.

In summary, this paper has the following contributions:

- We propose a new coarse-to-fine perspective to fuse RGB and IR features. Inspired by the mechanism of the human brain processing multimodal information, we coarsely remove the interfering information and finely select desired features for fusion.

- Following the coarse-to-fine fusion strategy, we propose a Redundant Spectrum Removal module, which introduces a dynamic spectrum filter to adaptively reduce irrelevant information in the frequency domain.
- We also design a Dynamic Feature Selection module, which utilizes a mixture of scale-aware experts to weigh different scale features for the RGB-IR feature fusion.
- To verify the effectiveness of the coarse-to-fine fusion strategy, we build a novel framework for RGB-IR object detection. Extensive experiments on three public RGB-IR object detection datasets demonstrate our proposed method achieves state-of-the-art performance.

II. RELATED WORKS

A. RGB-IR Object Detection

In recent years, thanks to the development of deep learning technology and several visible and infrared datasets being proposed [26]–[28], the RGB-IR object detection (also known as multispectral object detection) task has gradually attracted more and more attention. To fully explore the effective information between visible and infrared images, some researchers focus on the complementarity between the two modalities starting from the illumination conditions. Guan *et al.* [29] and Li *et al.* [30] first propose the illumination-aware modules to allow the object detectors to adjust the fusion weight based on the predicted illumination conditions. Moreover, Zhou *et al.* [21] analyze and address the modality imbalance problems by designing two feature fusion modules called DMAF and IAFA. Recently, an MSR memory module [31] was introduced to enhance the visual representation of the single modality features by recalling the RGB-IR modality features, which enables the detector to encode more discriminative features. Yuan *et al.* [32] propose a transformer-based RGB-IR object detector to further improve the object detector performance. Different from these works, We are inspired by the classic theory of cognitive psychology, Attenuation Theory, to emulate the way the human brain processes information from multiple sources. We propose a coarse-to-fine fusion strategy to fuse RGB and IR features for the RGB-IR object detection task.

B. Shared-Specific Representation Learning

Shared and specific representation learning is first explored in the Domain Separation Network [33] for unsupervised domain adaptation. It uses a shared-weight encoder to capture shared features and a private encoder to capture domain-specific features. Sanchez *et al.* [34] explored further shared and specific feature disentanglement representation, and found it is useful to perform downstream tasks such as image classification and retrieval. Recently, van *et al.* [35] improved the performance of action segmentation by disentangling the latent features into shared and modality-specific components. Furthermore, Wang *et al.* [36] proposed the ShaSpec model handled missing modalities problems. Shared-specific representation learning has shown great performance and effectiveness in feature learning. However, few RGB-IR object detection models explicitly exploit shared-specific representation. In this paper, we introduce shared-specific representation learning between RGB and IR modality features to implement our coarse-to-fine fusion strategy.

C. Mixture of Experts

The Mixture-of-Experts (MoE) model [37], [38] has demonstrated the ability to dynamically adapt its structure based on varying input conditions. Several studies have been dedicated to the theoretical exploration of MoE [39]–[42], focusing on the sparsity, training effectiveness, router mechanisms, enhancing model quality, etc. Besides, some researchers also concentrated on leveraging the MoE model for specific downstream tasks. For example, Gross *et al.* [43] observed that a hard mixture-of-experts model can be efficiently trained to good effect on large-scale multilabel prediction tasks. Cao *et al.* [44] proposed a mixture of local-to-global experts (MoE-Fusion) mechanisms by integrating MoE structure into image fusion tasks. Chen *et al.* [45] addressed the multi-task learning challenge by implementing a cooperative and specialized mechanism among experts. In our proposed method, the MoE model is integrated into the RGB-IR object detection task. Specifically, we establish multi-scale experts to gate modality features at different scales and leverage its dynamic fusion mechanism to facilitate complementary fusion.

III. METHOD

A. Coarse-to-Fine Fusion

The inspiration for the proposed ‘‘Coarse-to-Fine’’ Fusion strategy stems from the cognitive models of human processing of multiple sources of information, named Selective Attention Theory in cognitive psychology (e.g., ‘‘Broadbent’s filter model’’ [46] and ‘‘treisman’s Attenuation Model’’ [24]), which is one of the cornerstones of attention mechanism theory in cognitive psychology. The Selective Attention Theory posits that when the human brain processes multiple external stimuli, it first filters out or attenuates some unimportant or even useless information. Then, it further processes the information in a more refined manner before storing it in working memory, as illustrated in Figure 3. The Attenuating Filter corresponds to the Redundant Spectrum removal module (RSR), which effectively filters out unimportant or interfering information based

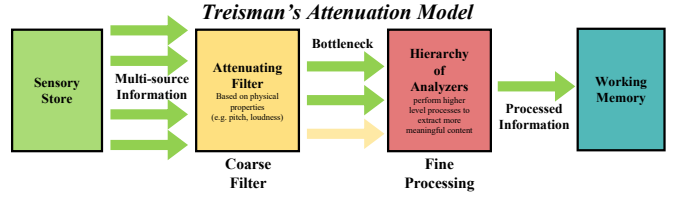


Fig. 3: Illustration of Treisman’s Attenuation Model

on some properties and rules when confronted with multi-sensory information. The Hierarchy of Analyzers corresponds to our proposed Dynamic Feature module (DFS), engaging in meticulous, higher-level analysis and processing to extract valuable insights. Finally, the processed information enters the brain’s working memory, corresponding to the output of the fused feature by our ‘‘Coarse-to-Fine Fusion’’ strategy and fed into the detection network.

According to the above inspiration, our ‘‘Coarse-to-Fine’’ Fusion strategy is designed as shown in Figure 4, ‘‘Coarse’’ corresponding to the Redundant Spectrum Removal (RSR) module to filter out coarsely in the frequency domain and ‘‘Fine’’ corresponding to the Dynamic Feature Selection (DFS) module to meticulously select the desired features between RGB-IR modalities. Since the two modality features are usually intersection, we introduce disentangled representation learning [34] to purify and decouple them for complementary fusion. Thus, we integrate the above two modules into the shared-specific structures to implement our coarse-to-fine fusion. Specifically, we first perform the RSR module to remove interfering information. Then, we introduce the shared-specific structure to extract the two modality-specific multiscale features $C_{I\text{-spe}}$ and $C_{V\text{-spe}}$, which uses ResNet50 [47] as the backbone network. As for the shared features C_{sha} , we also employ several Resblocks as the feature extractor. After that, these different scale features $C_{I\text{-spe}}$ and $C_{V\text{-spe}}$ are dynamically aggregated by the proposed mixture of scale-aware experts and obtain the final specific feature C_{spe} in the DFS module. Finally, the specific feature C_{spe} and the shared feature C_{sha} are added together for the final object detection task, which can be expressed as:

$$C = C_{\text{sha}} + C_{\text{spe}}. \quad (1)$$

B. Redundant Spectrum Removal

For the ‘‘Coarse Removal’’, since the frequency domain obeys the nature of global modeling, we propose a Redundant Spectrum Removal (RSR) module to filter out coarsely in the frequency domain. we first transform each source image into the frequency domain and predict a dynamic filter to adaptively reduce irrelevant spectrum within RGB and IR modalities. Specifically, the paired RGB image $V \in \mathbb{R}^{H \times W \times 3}$ and IR image $I \in \mathbb{R}^{H \times W \times 1}$ are taken as the RSR module input. They are first subjected to the Discrete Fourier Transform (DFT(\cdot)) and get the frequency domain image $F_I(u, v)$ and $F_V(u, v)$:

$$F_I(u, v) = \text{DFT}(I), \quad F_V(u, v) = \text{DFT}(V). \quad (2)$$

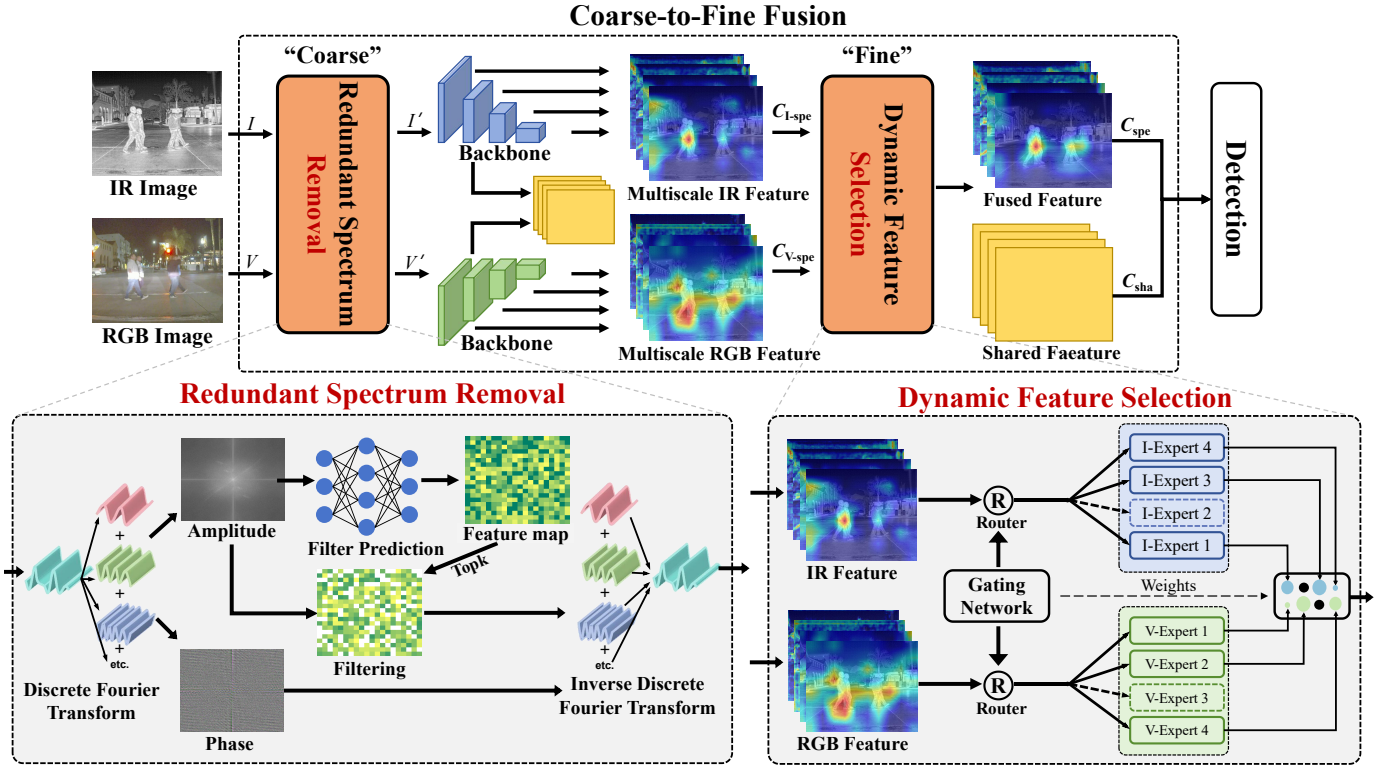


Fig. 4: The overall architecture of RSDet. The entire network follows the “Coarse-to-Fine” fusion and comprises a two-stream backbone network taking RGB and IR inputs, a Redundant Spectrum Removal (RSR) module, and a Dynamic Feature Selection (DFS) module.

The filter prediction network is conducted to dynamically generate the redundant spectrum filter, which is illustrated in Figure 4. For each modality image, we perform an embedding operation on the entire image get a feature vector, and reshape it to match the size of the original image:

$$\begin{aligned} M_{I_I} &= \text{Embed}(I), & M_{I_V} &= \text{Embed}(V), \\ M_{m_I} &= \text{Reshape}(M_{I_I}), & M_{m_V} &= \text{Reshape}(M_{I_V}). \end{aligned} \quad (3)$$

Then, for adaptively reducing irrelevant spectrum according to different inputs by the amplitude information of the original image, we utilize the top K operation on M_m . In specific, the positions don’t correspond to the top K values are set to 0:

$$H_I(u, v) = \text{top } K(M_{m_I}), H_V(u, v) = \text{top } K(M_{m_V}). \quad (4)$$

we apply $H(u, v)$ to filter the frequency domain image $F(u, v)$ for reducing irrelevant spectrum:

$$\begin{aligned} F'_I(u, v) &= F_I(u, v) \otimes H_I(u, v) \\ F'_V(u, v) &= F_V(u, v) \otimes H_V(u, v). \end{aligned} \quad (5)$$

Finally, the filtered $F'_I(u, v)$ and $F'_V(u, v)$ are subjected to the Inverse Discrete Fourier Transform $\text{IDFT}(\cdot)$ to transform the image back to the spatial domain. Thus, we obtain the final irrelevant spectrum removed images I' and V' .

$$I' = \text{IDFT}(F'_I(u, v)), V' = \text{IDFT}(F'_V(u, v)). \quad (6)$$

C. Dynamic Feature Selection

For the “Fine Selection”, we implement the dynamic modality feature selection in the fusion process by employing a

mixture of scale-aware experts to gate multi-scale features. As shown in Figure 4, we design a dedicated expert for each scale modality-specific feature. Then, we aggregate these features by using the gating network to predict a set of dynamic weights. Specifically, after obtaining different scale features $C_{I\text{-spe}}^i$ and $C_{V\text{-spe}}^i$ through the feature extraction for I' and V' , we first make $C_{I\text{-spe}}^i$ and $C_{V\text{-spe}}^i$ go through the average pooling operations, and flattened them into one-dimension vector $X_I^i \in \mathbb{R}^M$ and $X_V^i \in \mathbb{R}^M$ to predict the weights w_I^i and w_V^i of the gating network G . It can be formulated as follows:

$$w_I^i, w_V^i = G(X_I^i, X_V^i) = \text{Softmax}([X_I^i, X_V^i] \cdot W), \quad (7)$$

where the $W \in \mathbb{R}^{M \times N}$ is the learnable weight matrix normalized through the softmax operation and i is the index of experts. After that, the weights w_I and w_V are converted to gating via the Router R , preserving the desired features between the two modalities for fusion at different scales. Consequently, the Router R can be formulated as follows:

$$(r_I^i, r_V^i) = R(w_I^i, w_V^i) = \begin{cases} (1, 1), & w_I^i, w_V^i \geq t \\ (1, 0), & w_I^i \geq t, w_V^i \leq t, \\ (0, 1), & w_I^i \leq t, w_V^i \geq t \end{cases} \quad (8)$$

where t is a threshold. Then N scale-aware expert networks \mathcal{E}_I^i and \mathcal{E}_V^i are utilized to further extract modality-specific features. The formalization is as follows:

$$C_I^i = \mathcal{E}_I^i(x_I^i \cdot r_I^i), C_V^i = \mathcal{E}_V^i(x_V^i \cdot r_V^i), \quad (9)$$

where x_I^i and x_V^i are the multiscale features of different modality input I' and V' . The detailed structure of each

scale-aware expert \mathcal{E} is the same and mainly consists of two convolution blocks. After obtaining the output results from expert models at different scales, we perform dynamic weighted summation and concatenate them together to get the ultimate multi-modal specific feature C_{spe} :

$$C_{\text{spe}} = \bigcup_{i=1}^n (w_I^i C_I^i + w_V^i C_V^i). \quad (10)$$

D. Removal and Selection Detector (RSDet)

To evaluate the effectiveness of our Coarse-to-Fine fusion strategy, we embed it into an existing object detection framework. In specific, we utilize a two-stage detector Faster R-CNN [48] as our base model and replace its backbone with our strategy to construct a new object detector called RSDet. Other modules such as Region Proposal Network (RPN) and RoI head remain unchanged.

Loss functions. To extract the shared and specific feature from the images I' and V' , we maximize the mutual information between $C_{I\text{-spe}}$ and $C_{V\text{-spe}}$ with C_{sha} . The mutual information can serve as the deep supervising loss function $\mathcal{L}_{I\text{-spe}}$ and $\mathcal{L}_{V\text{-spe}}$ to guide the shared-specific features learning. The definitions are as follows:

$$\mathcal{L}_{I\text{-spe}} = \text{MI}(C_{\text{sha}}, C_{I\text{-spe}}), \quad (11)$$

$$\mathcal{L}_{V\text{-spe}} = \text{MI}(C_{\text{sha}}, C_{V\text{-spe}}), \quad (12)$$

where MI represents the operation of mutual information. We use cross-entropy (CE) and KL-divergence (KL) to approximate equivalent optimize the mutual information [49], [50] between different features in the latent space.

$$\max \text{MI}(x, y) \Rightarrow \max \{ \text{CE}(x, y) - \text{KL}(x||y) + \text{CE}(y, x) - \text{KL}(y||x) \}. \quad (13)$$

For detection loss, we also use the \mathcal{L}_{rpn} , \mathcal{L}_{reg} and \mathcal{L}_{cls} same as the Faster R-CNN [48] to supervise the training of whole Removal and Selection Detector. Thus, the total loss is the sum of these individual losses:

$$\mathcal{L} = \gamma(\mathcal{L}_{I\text{-spe}} + \mathcal{L}_{V\text{-spe}}) + \mathcal{L}_{\text{rpn}} + \mathcal{L}_{\text{reg}} + \mathcal{L}_{\text{cls}}, \quad (14)$$

where $\gamma = 0.001$ is the coefficient used to strike a balance between the different loss functions.

IV. EXPERIMENTS

A. Datasets

1) *KAIST Dataset*: KAIST [26] is a public multispectral pedestrian detection dataset. Due to the problematic annotations in the original dataset, our framework is trained on 8963 image pairs with new annotations [53] and evaluated on 2252 image pairs with the improved annotations [18]. To comprehensively evaluate the performance of our method, we perform comparison experiments under ‘All-dataset’ settings [26] and six subset datasets in terms of different pedestrian distances containing ‘Near’, ‘Medium’, and ‘Far’ and different occlusion levels containing ‘None’, ‘Partial’, and ‘Heavy’.

2) *FLIR-aligned Dataset*: FLIR is a paired visible and infrared object detection dataset including daytime and night scenes. Since the images are misaligned in the original dataset, we use the FLIR-aligned dataset [27]. It has 5142 aligned RGB-IR image pairs, of which 4129 are used for training and 1013 for testing, and contains three classes of objects: ‘person’, ‘car’, and ‘bicycle’. Since there are very few instances of the ‘dog’ category in the FLIR-aligned dataset, we clean the annotations and remove the ‘dog’ category from the dataset.

3) *LLVIP Dataset*: LLVIP [28] is a strictly aligned visible and infrared object detection dataset for low-light vision. It is collected in low-light environments most of which were captured in very dark scenes. It contains 15488 aligned RGB-IR image pairs, of which 12025 images are used for training and 3463 images for testing.

B. Evaluation Metrics

1) *Log-average Miss Rate (MR²)*: For the KAIST dataset, we employ the standard KAIST evaluation [26]: Miss Rate (MR) over False Positive Per Image (also denoted as MR²). It calculates the average miss rate under the 9 FPPI values which are sampled uniformly in the logarithmic interval. The lower values indicate better performance.

2) *Average Precision (AP)*: For FLIR and LLVIP datasets, we employ the commonly used object detection metric Average Precision (AP). The positive and negative samples should be divided according to the correctness of classification and Intersection over the Union (IoU) threshold. The mean Average Precision (mAP) represents the average of AP under all categories. The mAP₅₀ metric represents the mean AP under IoU=0.50 and The mAP metric represents the mean AP under IoU ranges from 0.50 to 0.95 with a stride of 0.05. The higher value of the mAP metrics means better performance.

C. Implementation Details

All the experiments are implemented in the mmdetection [62] toolbox and conducted on a single GPU NVIDIA GeForce RTX 3090. We use ResNet-50 as the backbone. During training, the batch size is set to 4 and the SGD optimizer is employed with a momentum of 0.9 and the weight decay of 1×10^{-4} . The input image resolution is 640×512 for FLIR and KAIST and 1280×1024 for LLVIP. All experiments are trained for 12 epochs with an initial learning rate of 1×10^{-2} . We use random flipping with a probability of 0.5 to increase input diversity.

D. Comparison with State-of-the-Art Methods

1) *Comparison on the KAIST Dataset*: The experiments are conducted on the KAIST under ‘All-dataset’ settings [19], [26]. We compare the proposed RSDet with twelve SOTA multispectral object detection methods on the KAIST dataset. As shown in Table I, We calculate the MR² at IoU values of 0.5 and 0.7, respectively.

When IoU=0.5, according to Table I(a), the RSDet performs best on the ‘All’, ‘Day’, and ‘Night’ conditions and the other four of six subsets (‘Near’, ‘Medium’, ‘Far’, ‘None’).

TABLE I: Detection results (MR^{-2} , in%) under ‘All-dataset’ settings of different pedestrian distances, occlusion levels, and light conditions (Day and Night) on the KAIST dataset. The pedestrian distances consist of ‘Near’ ($115 \leq height$), ‘Medium’ ($45 \leq height < 115$) and ‘Far’ ($1 \leq height < 45$), while occlusion levels consist of ‘None’ (never occluded), ‘Partial’ (occluded to some extent up to half) and ‘Heavy’ (mostly occluded). IoU = 0.5 / 0.7 is set for evaluation. The best results are highlighted in **red** and the second-place are highlighted in **blue**.

(a) IoU=0.5

Methods	Backbone	MR^{-2} (IoU=0.5)							Day	Night	All
		Near	Medium	Far	None	Partial	Heavy				
ACF [26]	VGG16	28.74	53.67	88.20	62.94	81.40	88.08	64.31	75.06	67.74	
Halfway Fusion [18]	VGG16	8.13	30.34	75.70	43.13	65.21	74.36	47.58	52.35	49.18	
FusionRPN+BF [51]	VGG16	0.04	30.87	88.86	47.45	56.10	72.20	52.33	51.09	51.70	
IAF R-CNN [30]	VGG16	0.96	25.54	77.84	40.17	48.40	69.76	42.46	47.70	44.23	
IATDNN+IASS [29]	VGG16	0.04	28.55	83.42	45.43	46.25	64.57	49.02	49.37	48.96	
CIAN [52]	VGG16	3.71	19.04	55.82	30.31	41.57	62.48	36.02	32.38	35.53	
MSDS-R-CNN [19]	VGG16	1.29	16.19	63.73	29.86	38.71	63.37	32.06	38.83	34.15	
AR-CNN [53]	VGG16	0.00	16.08	69.00	31.40	38.63	55.73	34.36	36.12	34.95	
MBNet [21]	ResNet50	0.00	16.07	55.99	27.74	35.43	59.14	32.37	30.95	31.87	
TSFADet [13]	ResNet50	0.00	15.99	50.71	25.63	37.29	65.67	31.76	27.44	30.74	
CMPD [17]	ResNet50	0.00	12.99	51.22	24.04	33.88	59.37	28.30	30.56	28.98	
CAGTDet [32]	ResNet50	0.00	14.00	49.40	24.48	33.20	59.35	28.79	27.73	28.96	
RSDet (Ours)	ResNet50	0.00	12.13	39.80	20.49	33.25	57.60	25.83	26.48	26.02	

(b) IoU=0.7

Methods	Backbone	MR^{-2} (IoU=0.7)							Day	Night	All
		Near	Medium	Far	None	Partial	Heavy				
ACF [26]	VGG16	79.25	82.96	97.86	87.59	94.61	97.86	88.48	92.47	89.54	
Halfway Fusion [18]	VGG16	49.59	74.87	97.00	80.35	90.42	94.15	81.31	86.34	83.15	
FusionRPN+BF [51]	VGG16	35.78	68.82	99.38	76.29	86.80	92.47	76.98	83.71	79.30	
IAF R-CNN [30]	VGG16	33.75	70.24	98.12	76.74	84.58	93.69	77.02	84.38	79.59	
IATDNN+IASS [29]	VGG16	45.40	70.85	99.00	78.25	84.51	93.13	80.46	82.32	80.91	
CIAN [52]	VGG16	38.31	63.98	87.12	70.39	80.95	91.68	72.44	78.92	74.45	
MSDS-R-CNN [19]	VGG16	35.49	57.95	93.15	68.41	76.23	90.37	69.85	78.52	71.93	
AR-CNN [53]	VGG16	25.19	53.88	91.72	64.91	73.18	88.70	64.45	77.29	68.64	
MBNet [21]	ResNet50	16.98	51.21	85.33	60.84	69.59	86.22	63.50	67.76	65.14	
TSFADet [13]	ResNet50	19.50	49.32	81.90	58.93	72.09	87.10	61.78	68.38	63.85	
CMPD [17]	ResNet50	19.31	49.69	83.93	59.79	66.64	84.79	61.77	68.83	63.93	
CAGTDet [32]	ResNet50	20.80	47.40	78.31	56.95	67.39	85.11	60.24	65.45	61.71	
RSDet (Ours)	ResNet50	12.68	46.73	73.95	55.35	65.03	84.08	59.72	62.46	60.65	

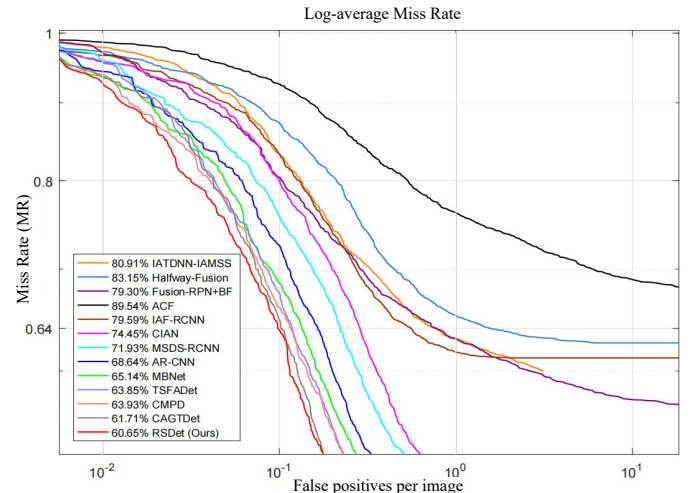
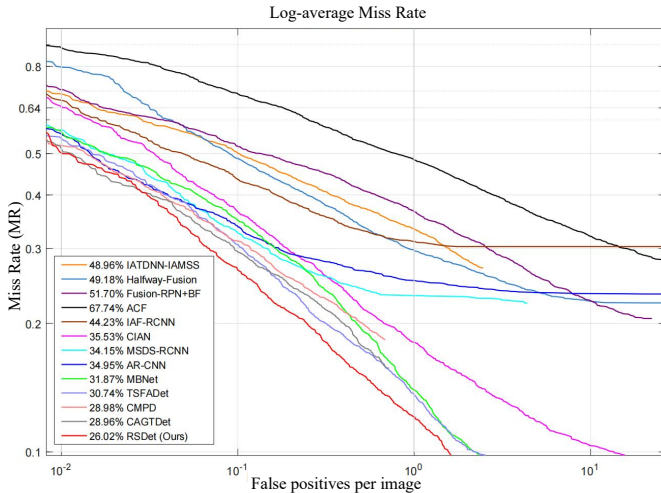


Fig. 5: The FPPI-MR curves comparisons with the state-of-the-art methods on the KAIST dataset under the ‘All-dataset’ settings [26].

TABLE II: Comparison the performance (mAP, in%) on the FLIR and LLVIP dataset. The best results are highlighted in **red** and the second-place are highlighted in **blue**.

Methods	Backbone	FLIR		LLVIP		Modality
		mAP ₅₀ ↑	mAP ↑	mAP ₅₀ ↑	mAP ↑	
SSD [54]	VGG16	65.5	29.6	90.2	53.5	IR
RetinaNet [55]	ResNet50	66.1	31.5	94.8	55.1	
Cascade R-CNN [56]	ResNet50	71.0	34.7	95.0	56.8	
Faster R-CNN [48]	ResNet50	74.4	37.6	94.6	54.5	
DDQ-DETR [57]	ResNet50	73.9	37.1	93.9	58.6	
SSD [54]	VGG16	52.2	21.8	82.6	39.8	RGB
RetinaNet [55]	ResNet50	51.2	21.9	88.0	42.8	
Cascade R-CNN [56]	ResNet50	56.0	24.7	88.3	47.0	
Faster R-CNN [48]	ResNet50	64.9	28.9	87.0	45.1	
DDQ-DETR [57]	ResNet50	64.9	30.9	86.1	46.7	
Halfway fusion [18]	VGG16	71.5	35.8	91.4	55.1	RGB+IR
GAFF [58]	ResNet18	74.6	37.4	94.0	55.8	
ProbEn [59]	ResNet50	75.5	37.9	93.4	51.5	
LGADet [60]	ResNet50	74.5	-	-	-	
CSAA [61]	ResNet50	79.2	41.3	94.3	59.2	
RSDet (Ours)	ResNet50	81.1	41.4	95.8	61.3	

TABLE III: Ablation study on each module result (mAP, in%) on the FLIR and LLVIP dataset. The best results are highlighted in **bold**.

RSR	DFS	FLIR		LLVIP	
		mAP ₅₀	mAP	mAP ₅₀	mAP
		75.2	37.2	95.0	55.5
✓		76.3	38.4	95.0	57.1
	✓	79.8	40.8	95.6	59.5
✓	✓	81.1	41.4	95.8	61.3

And rank second in two subsets (Partial and Heavy). Specifically, the RSDet takes the lead in the subsets of different scales (‘None’, ‘Medium’, ‘Far’), especially in the ‘Far’ subsets, the RSDet surpasses the second-best by about 10%, which is attributed to the mixture of scale-aware experts in the DFS module, Enhancing perceptual ability for targets at different distances. Besides, on the whole test dataset (‘All’), the RSDet surpasses the second-best by about 3%, which indicates the satisfactory accuracy of RSDet. The Log-average Miss Rate over the False Positive Per Image (FPPI) curve of all detectors under IoU=0.5 is shown in Figure 5(a).

When IoU=0.7, according to Table I(b), the RSDet performs best on all the different settings. As IoU increases, the requirement for detection accuracy becomes higher. In this scenario, the superiority of our method becomes even more pronounced. For instance, when IoU is 0.5, all the recent years’ methods MR is 0 under the ‘Near’ subset. However, when IoU increases to 0.7, the miss rate of other methods increases more significantly than RSDet, indicating that our proposed method detection results more accurately. The Log-average Miss Rate over the False Positive Per Image (FPPI) curve of all detectors under IoU=0.7 is also shown in Figure 5(b). The above experiment results on the KAIST dataset prove the superiority of our method.

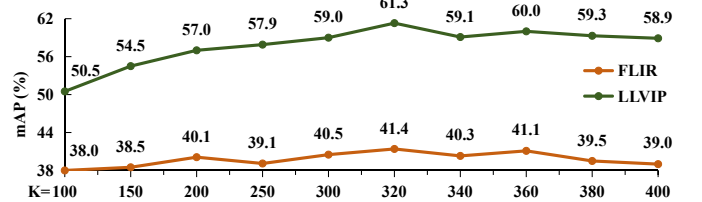


Fig. 6: Ablation study on different value K in RSR module on the FLIR and LLVIP dataset.

2) *Comparison on the FLIR and LLVIP Dataset:* The quantitative results of the different methods on the FLIR and LLVIP datasets are shown in Table II. We compare the proposed RSDet with five SOTA multispectral object detection methods and five single-modality object detection methods. From Table II, it can be observed that the experimental results of fusion methods are generally better than those of single-modal methods in the FLIR dataset. However, due to the limited light conditions, the RGB features interfere with the IR features in the LLVIP dataset, resulting in the detection results of the multispectral detector being inferior to the IR modality. However, our method effectively addresses this issue with the well-designed coarse-to-fine fusion strategy and achieves state-of-the-art performance on the both FLIR and LLVIP datasets.

E. Ablation Study

1) *Ablation on each component:* To verify the effectiveness of the RSR and DFS modules, we ablate each module from RSDet. As shown in Table III, only by adding the RSR module does the performance increase by 1.2% mAP on the FLIR dataset and 1.6% mAP on the LLVIP dataset respectively, and by only adding the DFS module, the metrics show a significant increase on the FLIR and LLVIP dataset, the performance increase by 3.6% mAP on the FLIR dataset and 4.0% mAP on the LLVIP dataset, respectively. Further adding both the

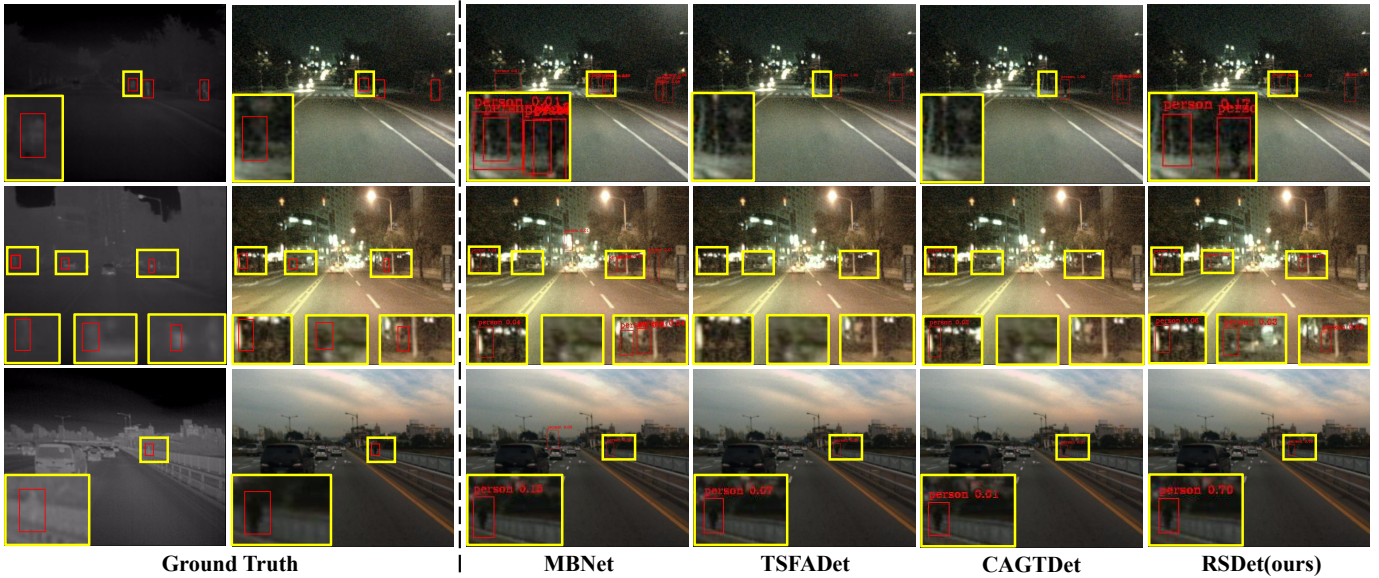


Fig. 7: Qualitative comparison of RSDet with other SOTA methods on the Kaist datasets. From left to right are the Ground Truth on IR and RGB image, MBNet [21], TSFADet [13], CAGTDet [32] and Ours.

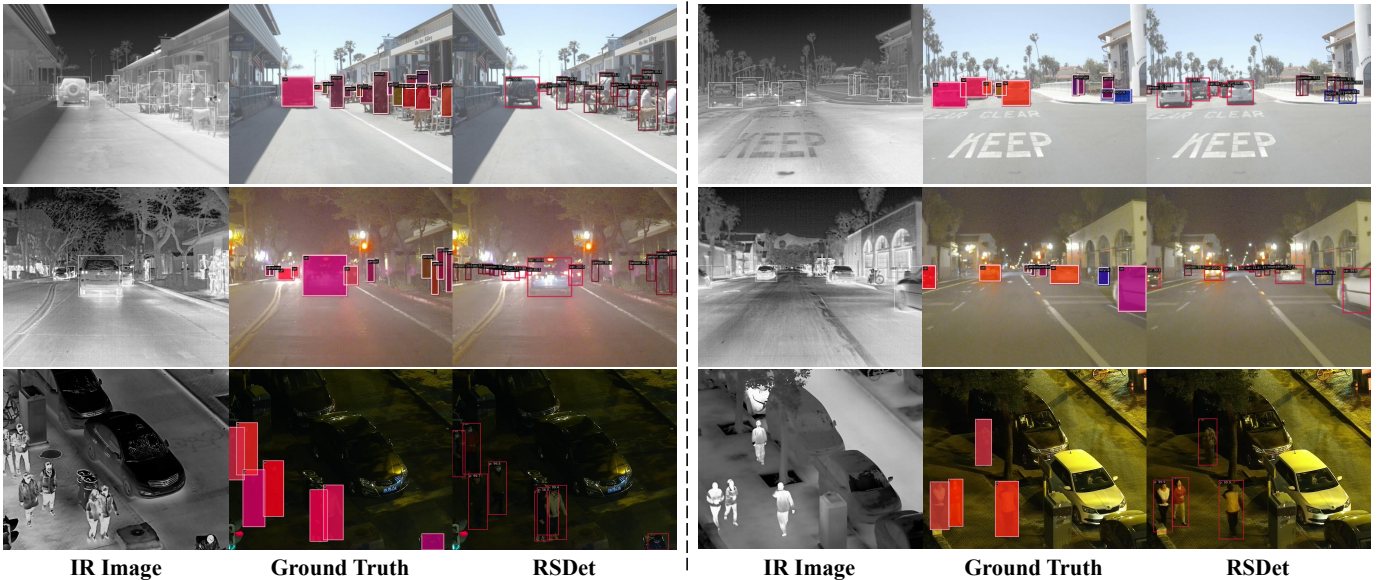


Fig. 8: Visualization of detection results of our method. The first two rows are from the FLIR dataset and the last row is from the LLVIP dataset. From left to right are the infrared image, the Ground Truth bounding box, and our detection results.

RSR and DFS modules, the metrics achieve the best level. The above results indicate the effectiveness of these modules.

2) *Ablation on different K* : We further study the impact of different values of K in the RSR module. We conduct the experiments by modifying the value of K ranging from 100 to 400 on the FLIR and LLVIP datasets. As shown in Figure 6, our detector achieves the highest detection performance when $K = 320$. If the value of K is increased or decreased, the performance of the detector will decrease, which also proves the negative impact of the redundant spectrum for the detector.

F. Visualization Results

1) *Kaist dataset*: We also visualize the object detection results of our RSDet with other state-of-the-art methods on the Kaist testing dataset. From the first two rows of Figure 7,

a common issue observed across the MBNet [21], TSFADet [13] and CAGTDet [32] methods is the missed detection of small objects. These results underscore the effectiveness of our DFS module, which can dynamically select different scale features between two modalities. Besides, by cooperating with the RSR module, our method can extract object features more effectively under complex lighting conditions and improve the performance of the detector, which is reflected in the confidence of the bounding box in the last row of Figure 7. The above results verify the effectiveness of our method.

2) *FLIR and LLVIP dataset*: In Figure 8, we visualize the object detection results of our method on the FLIR and LLVIP testing dataset. From Figure 8, we can see that our detection results include almost all bounding boxes of the Ground Truth labels with a high degree of consistency.

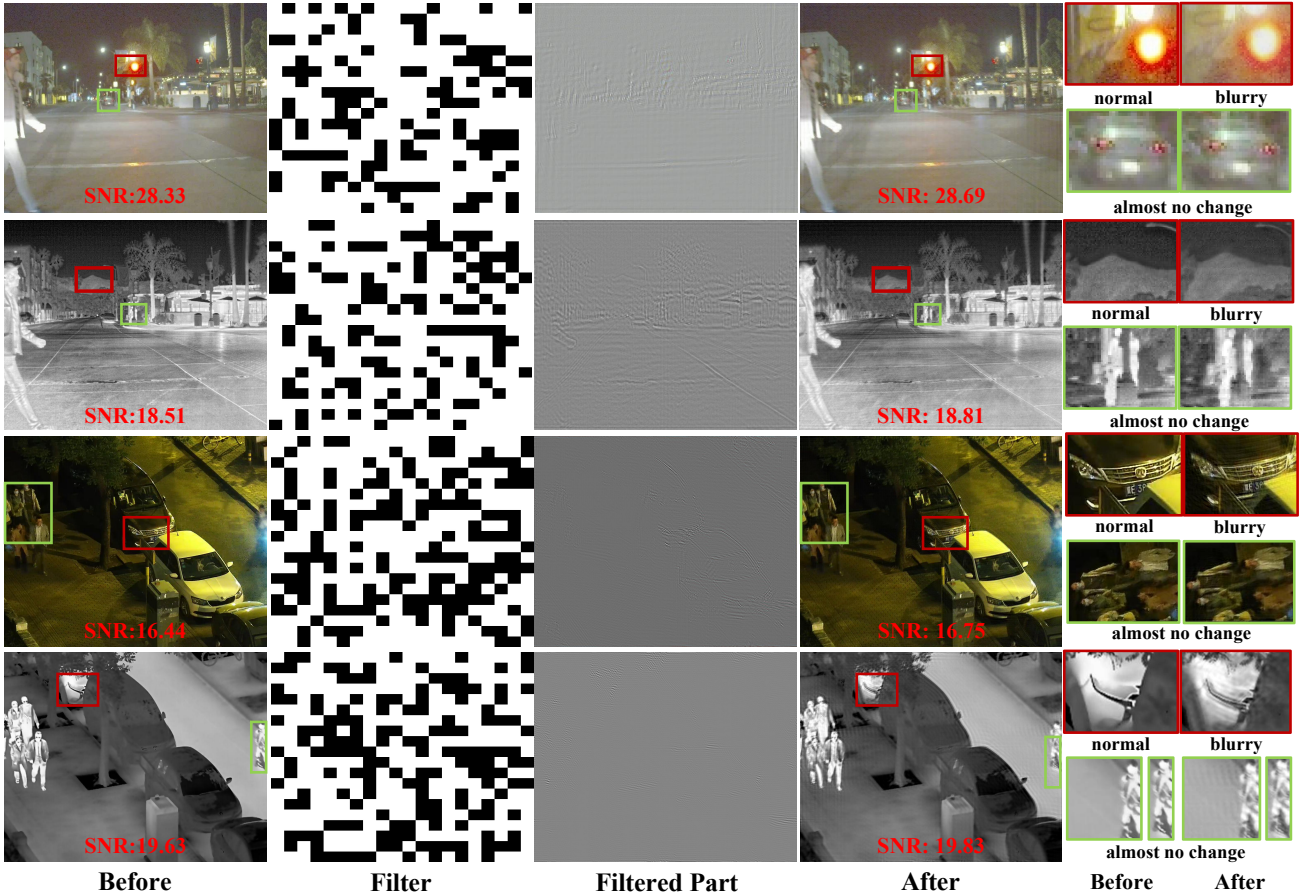


Fig. 9: Example of intermediate results of RSR module on FLIR (1,2 rows) and LLVIP (3,4 rows) datasets. “Before” represents the input images, “After” represents the filtered image after the RSR module, and “SNR” is the signal-to-noise ratio. We further visualize the learned filter and the filtered image content in the second column and third column respectively. The last column is the comparison of the background and the foreground region.

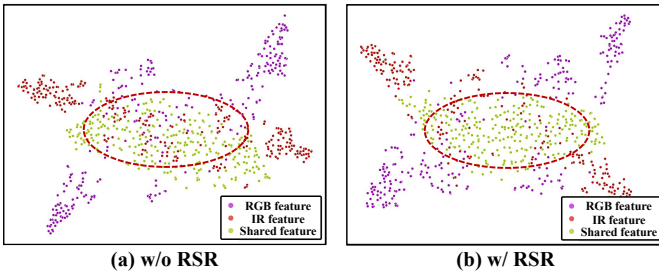


Fig. 10: tSNE visualization [63] of the modality-specific and shared features. (a) ‘w/o RSR’ represents without RSR module. (b) ‘w RSR’ represents with RSR module.

Furthermore, our method can also detect some small objects that are miss-labeled in the Ground Truth, which demonstrates the superiority of our method in multi-scale object detection.

3) *RSR module*: We visualize the intermediate results of the RSR module as shown in Figure 9. The second column visualizes the filter used in the frequency domain. Intuitively, both high- and low-frequency information will be filtered. We further transform the filtered information into the spatial domain, visualized in the third column. We can find that the removed information is mainly concentrated in the background region, which illustrates that the RSR module filters out some background redundant noise irrelevant to the detection task.

For further objective comparison, we use the signal-to-noise ratio (SNR) to measure the differences, which is calculated using the variance method: $SNR = 20 \times \log(\frac{\mu}{\sigma^2})$. It can be observed that SNR increases after using the RSR module, indicating the effectiveness of the RSR module.

We also conduct tSNE visualizations [63] of shared C_{sha} and specific features (C_{I-spe} and C_{V-spe}) on FLIR dataset. As shown in Figure 10, we have observed that without the RSR module, there is still a considerable mix of feature points in the shared and specific features, leading to difficulty in selecting the desired specific features in DFS. After adding the RSR module, we have noted a significant decrease in the number of mixed features, which verifies that removing redundant spectra is beneficial to feature disentanglement and, thus more effective in obtaining fused features in the DFS module.

4) *DFS module*: As shown in Figure 11, we visualize the shared and specific feature (C_{I-spe} , C_{V-spe} and C_{sha}) of different RGB-IR image pairs. We use red boxes to highlight the objects. By comparing the features before and after fusion, we observe that our fusion method makes non-salient objects in the shared feature become salient through the DFS module, and the fused features of our method are more prominent for the objects compared to other individual features.

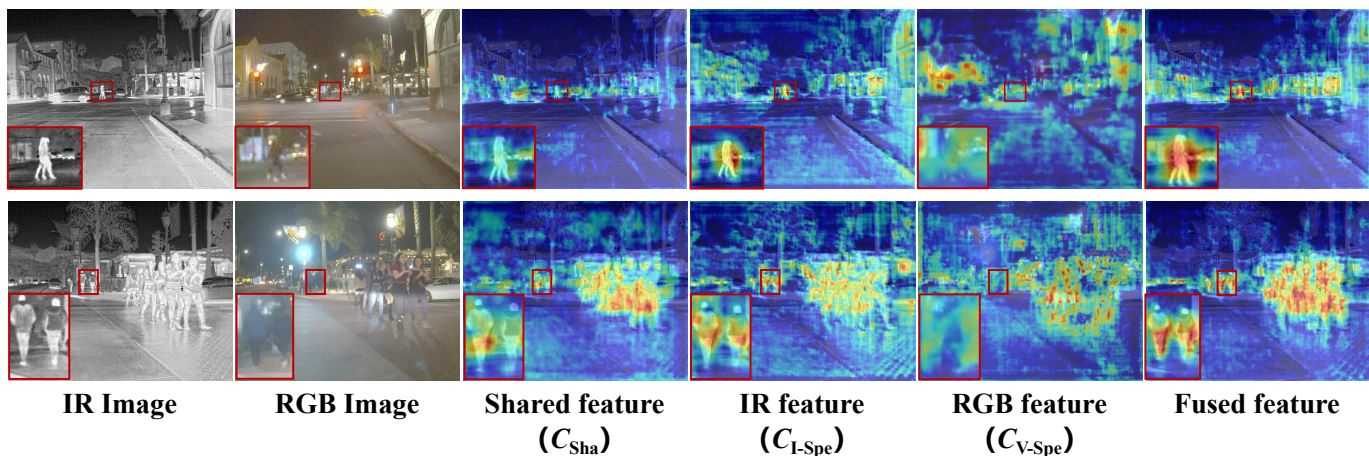


Fig. 11: Visualization of DFS module feature fusion results on the FLIR dataset. To facilitate a clearer observation, we overlaid the features onto the original RGB or IR image.

V. CONCLUSION

In this paper, we presented a new coarse-to-fine perspective to fuse visible and infrared modality features. Specifically, a Redundant Spectrum Removal (RSR) module is first designed to coarsely filter out the irrelevant spectrum, and then a Dynamic Feature Selection (DFS) module is proposed to finely select the desired features for the RGB-IR final feature fusion process. We constructed a new object detector called Removal and Selection Detector (RSDet) to evaluate its effectiveness and versatility. Extensive experiments on three public RGB-IR detection datasets demonstrated that our method can effectively facilitate complementary fusion and achieve state-of-the-art performance. We believe that our method can be applied to various studies in the RGB-IR feature fusion tasks.

REFERENCES

- [1] L. Wen, D. Du, Z. Cai, Z. Lei, M.-C. Chang, H. Qi, J. Lim, M.-H. Yang, and S. Lyu, "Ua-detrac: A new benchmark and protocol for multi-object detection and tracking," *Computer Vision and Image Understanding*, vol. 193, p. 102907, 2020.
- [2] J. Nascimento and J. Marques, "Performance evaluation of object detection algorithms for video surveillance," *IEEE Transactions on Multimedia*, vol. 8, no. 4, pp. 761–774, 2006.
- [3] B. Li, X. Xiaoyang, W. Xingxing, and T. Wenting, "Ship detection and classification from optical remote sensing images: A survey," *Chinese Journal of Aeronautics*, vol. 34, no. 3, pp. 145–163, 2021.
- [4] G.-S. Xia, X. Bai, J. Ding, Z. Zhu, S. Belongie, J. Luo, M. Datcu, M. Pelillo, and L. Zhang, "Dota: A large-scale dataset for object detection in aerial images," in *Proceedings of the IEEE conference on computer vision and pattern recognition*, 2018, pp. 3974–3983.
- [5] H. Yan, B. Li, H. Zhang, and X. Wei, "An antijamming and lightweight ship detector designed for spaceborne optical images," *IEEE Journal of Selected Topics in Applied Earth Observations and Remote Sensing*, vol. 15, pp. 4468–4481, 2022.
- [6] Y. Wei, L. Zhao, W. Zheng, Z. Zhu, J. Zhou, and J. Lu, "Surroundocc: Multi-camera 3d occupancy prediction for autonomous driving," in *Proceedings of the IEEE/CVF International Conference on Computer Vision*, 2023, pp. 21 729–21 740.
- [7] F. Yu, H. Chen, X. Wang, W. Xian, Y. Chen, F. Liu, V. Madhavan, and T. Darrell, "Bdd100k: A diverse driving dataset for heterogeneous multitask learning," in *Proceedings of the IEEE/CVF conference on computer vision and pattern recognition*, 2020, pp. 2636–2645.
- [8] X. Wei and S. Zhao, "Boosting adversarial transferability with learnable patch-wise masks," *IEEE Transactions on Multimedia*, 2023.
- [9] J. U. Kim, S. Park, and Y. M. Ro, "Uncertainty-guided cross-modal learning for robust multispectral pedestrian detection," *IEEE Transactions on Circuits and Systems for Video Technology*, vol. 32, no. 3, pp. 1510–1523, 2021.
- [10] S. Song, Z. Miao, H. Yu, J. Fang, K. Zheng, C. Ma, and S. Wang, "Deep domain adaptation based multi-spectral salient object detection," *IEEE Transactions on Multimedia*, vol. 24, pp. 128–140, 2022.
- [11] Z. Xie, F. Shao, G. Chen, H. Chen, Q. Jiang, X. Meng, and Y.-S. Ho, "Cross-modality double bidirectional interaction and fusion network for rgb-t salient object detection," *IEEE Transactions on Circuits and Systems for Video Technology*, 2023.
- [12] K. Wang, Z. Tu, C. Li, C. Zhang, and B. Luo, "Learning adaptive fusion bank for multi-modal salient object detection," *IEEE Transactions on Circuits and Systems for Video Technology*, 2024.
- [13] M. Yuan, Y. Wang, and X. Wei, "Translation, scale and rotation: Cross-modal alignment meets rgb-infrared vehicle detection," in *European Conference on Computer Vision*. Springer, 2022, pp. 509–525.
- [14] Y. Sun, B. Cao, P. Zhu, and Q. Hu, "Drone-based rgb-infrared cross-modality vehicle detection via uncertainty-aware learning," *IEEE Transactions on Circuits and Systems for Video Technology*, vol. 32, no. 10, pp. 6700–6713, 2022.
- [15] M. Yuan and X. Wei, "C²former: Calibrated and complementary transformer for rgb-infrared object detection," *arXiv preprint arXiv:2306.16175*, 2023.
- [16] Q. Li, C. Zhang, Q. Hu, P. Zhu, H. Fu, and L. Chen, "Stabilizing multispectral pedestrian detection with evidential hybrid fusion," *IEEE Transactions on Circuits and Systems for Video Technology*, 2023.
- [17] Q. Li, C. Zhang, Q. Hu, H. Fu, and P. Zhu, "Confidence-aware fusion using dempster-shafer theory for multispectral pedestrian detection," *IEEE Transactions on Multimedia*, 2022.
- [18] J. Liu, S. Zhang, S. Wang, and D. N. Metaxas, "Multispectral deep neural networks for pedestrian detection," *arXiv preprint arXiv:1611.02644*, 2016.
- [19] C. Li, D. Song, R. Tong, and M. Tang, "Multispectral pedestrian detection via simultaneous detection and segmentation," in *British Machine Vision Conference (BMVC)*, 2018.
- [20] Y. Cao, D. Guan, Y. Wu, J. Yang, Y. Cao, and M. Y. Yang, "Box-level segmentation supervised deep neural networks for accurate and real-time multispectral pedestrian detection," *ISPRS journal of photogrammetry and remote sensing*, vol. 150, pp. 70–79, 2019.
- [21] K. Zhou, L. Chen, and X. Cao, "Improving multispectral pedestrian detection by addressing modality imbalance problems," in *Computer Vision—ECCV 2020: 16th European Conference, Glasgow, UK, August 23–28, 2020, Proceedings, Part XVIII 16*. Springer, 2020, pp. 787–803.
- [22] J. Xie, R. M. Anwer, H. Cholakkal, J. Nie, J. Cao, J. Laaksonen, and F. S. Khan, "Learning a dynamic cross-modal network for multispectral pedestrian detection," in *Proceedings of the 30th ACM International Conference on Multimedia*, 2022, pp. 4043–4052.
- [23] R. Li, J. Xiang, F. Sun, Y. Yuan, L. Yuan, and S. Gou, "Multiscale cross-modal homogeneity enhancement and confidence-aware fusion for multispectral pedestrian detection," *IEEE Transactions on Multimedia*, 2023.

- [24] A. M. Treisman, "Selective attention in man." *British medical bulletin*, 1964.
- [25] J. Li, L.-Y. Duan, X. Chen, T. Huang, and Y. Tian, "Finding the secret of image saliency in the frequency domain," *IEEE transactions on pattern analysis and machine intelligence*, vol. 37, no. 12, pp. 2428–2440, 2015.
- [26] S. Hwang, J. Park, N. Kim, Y. Choi, and I. So Kweon, "Multispectral pedestrian detection: Benchmark dataset and baseline," in *Proceedings of the IEEE conference on computer vision and pattern recognition*, 2015, pp. 1037–1045.
- [27] H. Zhang, E. Fromont, S. Lefevre, and B. Avignon, "Multispectral fusion for object detection with cyclic fuse-and-refine blocks," in *2020 IEEE International conference on image processing (ICIP)*. IEEE, 2020, pp. 276–280.
- [28] X. Jia, C. Zhu, M. Li, W. Tang, and W. Zhou, "Llvip: A visible-infrared paired dataset for low-light vision," in *Proceedings of the IEEE/CVF international conference on computer vision*, 2021, pp. 3496–3504.
- [29] D. Guan, Y. Cao, J. Yang, Y. Cao, and M. Y. Yang, "Fusion of multispectral data through illumination-aware deep neural networks for pedestrian detection," *Information Fusion*, vol. 50, pp. 148–157, 2019.
- [30] C. Li, D. Song, R. Tong, and M. Tang, "Illumination-aware faster r-cnn for robust multispectral pedestrian detection," *Pattern Recognition*, vol. 85, pp. 161–171, 2019.
- [31] J. U. Kim, S. Park, and Y. M. Ro, "Towards versatile pedestrian detector with multisensory-matching and multispectral recalling memory," in *Proceedings of the AAAI Conference on Artificial Intelligence*, vol. 36, 2022, pp. 1157–1165.
- [32] M. Yuan, X. Shi, N. Wang, Y. Wang, and X. Wei, "Improving rgb-infrared object detection with cascade alignment-guided transformer," *Information Fusion*, p. 102246, 2024.
- [33] K. Bousmalis, G. Trigeorgis, N. Silberman, D. Krishnan, and D. Erhan, "Domain separation networks," *Advances in neural information processing systems*, vol. 29, 2016.
- [34] E. H. Sanchez, M. Serrurier, and M. Ortner, "Learning disentangled representations via mutual information estimation," in *Computer Vision–ECCV 2020: 16th European Conference, Glasgow, UK, August 23–28, 2020, Proceedings, Part XXII 16*. Springer, 2020, pp. 205–221.
- [35] B. van Amsterdam, A. Kadkhodamohammadi, I. Luengo, and D. Stoyanov, "Aspnet: Action segmentation with shared-private representation of multiple data sources," in *Proceedings of the IEEE/CVF Conference on Computer Vision and Pattern Recognition*, 2023, pp. 2384–2393.
- [36] H. Wang, Y. Chen, C. Ma, J. Avery, L. Hull, and G. Carneiro, "Multi-modal learning with missing modality via shared-specific feature modelling," in *Proceedings of the IEEE/CVF Conference on Computer Vision and Pattern Recognition*, 2023, pp. 15 878–15 887.
- [37] R. A. Jacobs, M. I. Jordan, S. J. Nowlan, and G. E. Hinton, "Adaptive mixtures of local experts," *Neural computation*, vol. 3, no. 1, pp. 79–87, 1991.
- [38] M. I. Jordan and R. A. Jacobs, "Hierarchical mixtures of experts and the em algorithm," *Neural computation*, vol. 6, no. 2, pp. 181–214, 1994.
- [39] N. Shazeer, A. Mirhoseini, K. Maziarz, A. Davis, Q. Le, G. Hinton, and J. Dean, "Outrageously large neural networks: The sparsely-gated mixture-of-experts layer," *arXiv preprint arXiv:1701.06538*, 2017.
- [40] D. Lepikhin, H. Lee, Y. Xu, D. Chen, O. Firat, Y. Huang, M. Krikun, N. Shazeer, and Z. Chen, "{GS}hard: Scaling giant models with conditional computation and automatic sharding," in *International Conference on Learning Representations*, 2021. [Online]. Available: <https://openreview.net/forum?id=qrwe7XHTmYb>
- [41] X. Nie, S. Cao, X. Miao, L. Ma, J. Xue, Y. Miao, Z. Yang, Z. Yang, and B. CUI, "Dense-to-sparse gate for mixture-of-experts," 2022. [Online]. Available: https://openreview.net/forum?id=_4D8IVs7yO8
- [42] Y. Zhou, T. Lei, H. Liu, N. Du, Y. Huang, V. Zhao, A. M. Dai, Q. V. Le, J. Laudon *et al.*, "Mixture-of-experts with expert choice routing," *Advances in Neural Information Processing Systems*, vol. 35, pp. 7103–7114, 2022.
- [43] S. Gross, M. Ranzato, and A. Szlam, "Hard mixtures of experts for large scale weakly supervised vision," in *Proceedings of the IEEE Conference on Computer Vision and Pattern Recognition*, 2017, pp. 6865–6873.
- [44] B. Cao, Y. Sun, P. Zhu, and Q. Hu, "Multi-modal gated mixture of local-to-global experts for dynamic image fusion," in *Proceedings of the IEEE/CVF International Conference on Computer Vision*, 2023, pp. 23 555–23 564.
- [45] Z. Chen, Y. Shen, M. Ding, Z. Chen, H. Zhao, E. G. Learned-Miller, and C. Gan, "Mod-squad: Designing mixtures of experts as modular multi-task learners," in *Proceedings of the IEEE/CVF Conference on Computer Vision and Pattern Recognition*, 2023, pp. 11 828–11 837.
- [46] D. E. Broadbent, "Perception and communication," 1958.
- [47] K. He, X. Zhang, S. Ren, and J. Sun, "Deep residual learning for image recognition," in *Proceedings of the IEEE conference on computer vision and pattern recognition*, 2016, pp. 770–778.
- [48] S. Ren, K. He, R. Girshick, and J. Sun, "Faster r-cnn: Towards real-time object detection with region proposal networks," *IEEE Transactions on Pattern Analysis & Machine Intelligence*, vol. 39, no. 06, pp. 1137–1149, 2017.
- [49] A. Sanghi, "Info3d: Representation learning on 3d objects using mutual information maximization and contrastive learning," in *Computer Vision–ECCV 2020: 16th European Conference, Glasgow, UK, August 23–28, 2020, Proceedings, Part XXIX 16*. Springer, 2020, pp. 626–642.
- [50] M. Tschannen, J. Djolonga, P. K. Rubenstein, S. Gelly, and M. Lucic, "On mutual information maximization for representation learning," in *International Conference on Learning Representations*, 2019.
- [51] D. König, M. Adam, C. Jarvers, G. Layher, H. Neumann, and M. Teutsch, "Fully convolutional region proposal networks for multi-spectral person detection," in *Proceedings of the IEEE conference on computer vision and pattern recognition workshops*, 2017, pp. 49–56.
- [52] L. Zhang, Z. Liu, S. Zhang, X. Yang, H. Qiao, K. Huang, and A. Husain, "Cross-modality interactive attention network for multispectral pedestrian detection," *Information Fusion*, vol. 50, pp. 20–29, 2019.
- [53] L. Zhang, X. Zhu, X. Chen, X. Yang, Z. Lei, and Z. Liu, "Weakly aligned cross-modal learning for multispectral pedestrian detection," in *Proceedings of the IEEE/CVF international conference on computer vision*, 2019, pp. 5127–5137.
- [54] W. Liu, D. Anguelov, D. Erhan, C. Szegedy, S. Reed, C.-Y. Fu, and A. C. Berg, "Ssd: Single shot multibox detector," in *Computer Vision–ECCV 2016: 14th European Conference, Amsterdam, The Netherlands, October 11–14, 2016, Proceedings, Part I 14*. Springer, 2016, pp. 21–37.
- [55] T.-Y. Lin, P. Goyal, R. Girshick, K. He, and P. Dollár, "Focal loss for dense object detection," in *Proceedings of the IEEE international conference on computer vision*, 2017, pp. 2980–2988.
- [56] Z. Cai and N. Vasconcelos, "Cascade r-cnn: High quality object detection and instance segmentation," *IEEE transactions on pattern analysis and machine intelligence*, vol. 43, no. 5, pp. 1483–1498, 2019.
- [57] S. Zhang, X. Wang, J. Wang, J. Pang, C. Lyu, W. Zhang, P. Luo, and K. Chen, "Dense distinct query for end-to-end object detection," in *Proceedings of the IEEE/CVF Conference on Computer Vision and Pattern Recognition*, 2023, pp. 7329–7338.
- [58] H. Zhang, E. Fromont, S. Lefèvre, and B. Avignon, "Guided attentive feature fusion for multispectral pedestrian detection," in *Proceedings of the IEEE/CVF winter conference on applications of computer vision*, 2021, pp. 72–80.
- [59] Y.-T. Chen, J. Shi, Z. Ye, C. Mertz, D. Ramanan, and S. Kong, "Multimodal object detection via probabilistic ensembling," in *European Conference on Computer Vision*. Springer, 2022, pp. 139–158.
- [60] X. Zuo, Z. Wang, Y. Liu, J. Shen, and H. Wang, "Lgadet: Lightweight anchor-free multispectral pedestrian detection with mixed local and global attention," *Neural Processing Letters*, vol. 55, no. 3, pp. 2935–2952, 2023.
- [61] Y. Cao, J. Bin, J. Hamari, E. Blasch, and Z. Liu, "Multimodal object detection by channel switching and spatial attention," in *Proceedings of the IEEE/CVF Conference on Computer Vision and Pattern Recognition Workshops*, 2023, pp. 403–411.
- [62] K. Chen, J. Wang, J. Pang, Y. Cao, Y. Xiong, X. Li, S. Sun, W. Feng, Z. Liu, J. Xu *et al.*, "Mmdetection: Open mmlab detection toolbox and benchmark," *arXiv preprint arXiv:1906.07155*, 2019.
- [63] L. Van der Maaten and G. Hinton, "Visualizing data using t-sne." *Journal of machine learning research*, vol. 9, no. 11, 2008.